THE JOURNAL OF PHYSICAL CHEMISTRY C
A JOURNAL OF THE AMERICAN CHEMICAL SOCIETY

pubs.acs.org/JPCC

Article

Heterovalent Bi^{III}/Pb^{II} Ionic Substitution in One-Dimensional Trimethylsulfoxonium Halide Pseudo-Perovskites (X = I, Br)

Candida Pipitone, Francesco Giannici,* Antonino Martorana, Gonzalo García-Espejo, Silvia Carlotto, Maurizio Casarin, Antonietta Guagliardi, and Norberto Masciocchi*

Cite This: *J. Phys. Chem. C* 2021, 125, 11728–11742

Read Online

ACCESS | Metrics & More | Article Recommendations | Supporting Information

ABSTRACT: We report on the synthesis and characterization of novel lead and bismuth hybrid (organic–inorganic) iodide and bromide pseudo-perovskites (ABX_3) containing the trimethylsulfoxonium cation $(CH_3)_3SO^+$ (TMSO) in the A site, Pb/Bi in the B site, and Br or I as X anions. All of these compounds are isomorphic and crystallize in the orthorhombic *Pnma* space group. Lead-based pseudo-perovskites consist of one-dimensional (1D) chains of face-sharing $[PbX_6]$ octahedra, while in the bismuth-based ones, the chains of $[BiX_6]$ are interrupted, with one vacancy every third site, leading to a zero-dimensional (0D) local structure based on separated $[Bi_2I_9]^{3-}$ dimers. Five solid solutions for the iodide with different Pb^{2+}/Bi^{3+} ratios between $(TMSO)PbI_3$ and $(TMSO)_3Bi_2I_9$, and two for the bromide counterparts, were synthetized. Due to the charge compensation mechanism, these systems are best described by the $(TMSO)_3Pb_{3x}Bi_{2(1-x)}I_9$ (x = 0.98, 0.92, 0.89, 0.56, and 0.33) and $(TMSO)_3Pb_{3x}Bi_{2(1-x)}Br_9$ (x = 0.83 and 0.37) formulae. X-ray powder diffraction (XRPD) measurements were employed to determine the crystal structure of all studied species and further used to test the metal cation miscibility within monophasic samples not showing cation segregation. These systems can be described through an ionic defectivity on the pseudo-perovskite B site, where the Pb^{2+}/Bi^{3+} replacement is compensated by one Pb^{2+} vacancy for every Bi^{3+} pair. This leads to a wide range of possible different (numerical and geometrical) chain configurations, leading to the unique features observed in XRPD patterns. The optical band gap of the iodide samples falls in the 2.11–2.74 eV range and decreases upon increasing the Bi^{3+} content. Interestingly, even a very low loading of Bi^{3+} (1%) is sufficient to reduce the band gap substantially from 2.74 to 2.25 eV. Periodic density functional theory (DFT) calculations were used to simulate the atomic and electronic structures of our samples, with predicted band gap trends in good agreement with the experimental ones. This work highlights the structural flexibility of such systems and accurately interprets the ionic defectivity of the different pseudo-perovskite structures.

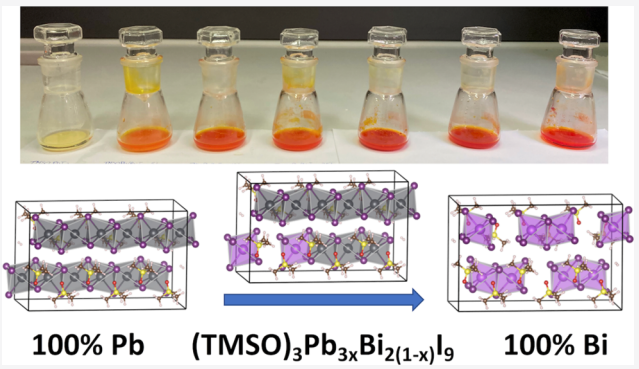

INTRODUCTION

Over the last two decades, halide-based perovskites have received significant attention from the wide materials chemistry community.[1,2] This is due to their attractive photophysical properties, which make this family of materials up-and-coming for green energy applications as photovoltaics, solar thermoelectrics, light-emitting diodes, field-effect transistors, lasers, and scintillators.[3−8] The most studied compounds of this family are formed by a three-dimensional network of corner-sharing metal halide octahedra, among which A^+ cations (either organic or inorganic or both) are hosted. They are formally described by the ABX_3 formula, where B^{2+} is the framework-forming cation and X^- the halide. For practical applications of these materials, there are still unresolved issues to be overcome, e.g., low stability to air, light, or moisture, low electrical conductivity, or inadequate band gaps.[4,9−12]

Recent research efforts are directed toward optimizing the properties of three-dimensional (3D) species by tuning the composition of the pristine compounds through the formation of mixed-cation and mixed-anion (or both) species, once a wide tolerance to the introduction of lattice defects had been discovered for many halide perovskites. For instance, $(CH_3NH_3)_{0.45}(HC(NH_2)_2)_{0.55}PbI_3$, in which the A^+ site is shared by methylammonium and formamidinium cations, is reported to have higher carrier mobility, longer diffusion length, and higher stability than any of the two $(CH_3NH_3)PbI_3$ and $(HC(NH_2)_2)PbI_3$ end members.[13] Similarly, doping of the anion site is widely reported as an effective way to modulate the band gap of the materials.[14] Finally, doping the B^{2+} metal site[15]

Received: March 22, 2021
Revised: May 3, 2021
Published: May 19, 2021

adds on an alternative approach to modifying the electronic and atomic structure. In this regard, aliovalent Bi^{3+} doping within Pb-based perovskites has recently been reported to increase the electrical conductivity up to 4 orders of magnitude while simultaneously decreasing the band gap.[16] Bi^{3+} doping was also reported to affect the optical properties of inorganic and hybrid lead halide perovskites.[15,17] Homovalent doping with Mn^{2+} was also successfully used to enhance the charge carrier mobility of the pristine lead-based materials.[18] Considering the doping-based observed versatility, we believe that there are still plenty of parameters to explore that can lead to different and alternative opportunities. These include structural, polymorphic, and compositional changes, with all three effects possibly leading to low-dimensional pseudo-perovskite materials characterized by diverse geometrical arrangements of the BX_6 octahedra. In these cases, the connectivity of these octahedra may be limited to two-dimensional (2D layers or slabs), one-dimensional (1D wires), or zero-dimensional (isolated octahedra) structural configurations,[19] or a combination thereof. Aiming at constructing devices with better performances, both 2D and 1D structures, together with 3D ones, have been used.[20−23] Despite this exciting scenario, doping of low-dimensional perovskites and its impact on functional properties are still poorly studied, with only a few reports dealing with layered materials.[24−29]

In this work, we focus on the preparation of two sets of hybrid pseudo-perovskites (I- and Br-based) containing trimethylsulfoxonium, $(CH_3)_3SO^+$ (TMSO), as the organic moiety, with Pb^{2+} or Bi^{3+} cations in the perovskite B site and their solid solutions. These systems were studied in depth through spectroscopic, thermal, structural, and density functional theory (DFT) characterization. Our syntheses led to the isolation of the following polycrystalline species: $(TMSO)PbI_3$, $(TMSO)PbBr_3$, $(TMSO)_3Bi_2I_9$, and $(TMSO)_3Bi_2Br_9$, hereafter denoted as "end members," the crystal structures of which were determined by ab initio structural analysis from X-ray powder diffraction (XRPD) data. The miscibility of Pb^{2+}/Bi^{3+} cations was investigated through the preparation of five solid solutions with iodide and two solid solutions with bromide. All mixed Pb/Bi samples were found to crystallize in a single phase. Peculiar diffraction peak shapes were found in most XRPD traces due to complex disorder patterns attributed to the short-range ordering of $Bi_{Pb}^{\bullet}$ and V_{Pb}''defects. All species show remarkable stability to oxygen, moisture, and temperature. The optical energy band gaps, E_g, of the materials were derived by UV−vis reflectance spectra and compared to those predicted by ab initio DFT calculations at the Perdew−Burke−Ernzerhof (PBE) level.

METHODS

Materials. Lead oxide (PbO, 99%), hydroiodic acid (HI, 57% w/w aqueous stabilized with 1.5 w/w H_3PO_2), hypophosphorous acid (H_3PO_2, 50% w/w aqueous solution), and trimethylsulfoxonium iodide ($((CH_3)_3SO)I$, >98%) were purchased from Alfa Aesar. Bismuth oxide (Bi_2O_3, 99.9%), hydrobromic acid (HBr, ACS reagent 48%), and anhydrous ethanol (C_2H_6O, >99%) were purchased from Sigma-Aldrich. Solid trimethylsulfoxonium bromide ($((CH_3)_3SO)Br$, 98%) was purchased from Tokyo Chemical Industry. All reagents were used as received.

Syntheses. *End Members. (TMSO)PbI$_3$.* PbO powder (1 mmol) was dissolved in 5 mL of HI and 1 mL of H_3PO_2. The solution was heated to 70 °C to dissolve all-lead oxide, resulting in a bright yellow solution. (TMSO)I powder (1 mmol) was added to the solution, causing the immediate precipitation of a light yellow powder. The solid was collected by filtration under vacuum and washed with anhydrous ethanol. Yield 87%.

(TMSO)PbBr$_3$. PbO powder (1 mmol) was dissolved in 6 mL of HBr by heating the solution up to 70 °C. (TMSO)Br powder (1 mmol) was added to the solution. The solution was left to evaporate on a heating plate until precipitation of a white polycrystalline solid occurred. The powders were collected by filtration under vacuum and washed with anhydrous ethanol. Yield 42%.

(TMSO)$_3$Bi$_2$I$_9$. Bi_2O_3 powder (0.5 mmol) was dissolved in 5 mL of HI and 1 mL of H_3PO_2. The solution was heated to 70 °C to dissolve all-bismuth oxide, resulting in a dark orange solution. (TMSO)I powder (1 mmol) was added to the solution, causing the immediate precipitation of a red powder. The solid was collected by filtration under vacuum and washed with anhydrous ethanol. Yield 81%.

(TMSO)$_3$Bi$_2$Br$_9$. Bi_2O_3 powder (0.5 mmol) was dissolved in 6 mL of HBr by heating the solution up to 70 °C. (TMSO)Br powder (1 mmol) was then added to the solution. The solution was left to evaporate on the heating plate until a light yellow polycrystalline solid precipitate occurred. The powders were collected by filtration under vacuum and washed with anhydrous ethanol. Yield 52%.

Solid Solutions. (TMSO)$_3$Pb$_{3x}$Bi$_{2(1−x)}$I$_9$ (0 < x < 1). PbO and Bi_2O_3 powders (mmol reported in Table S1 for each sample) were dissolved in 5 mL of HI and 1 mL of H_3PO_2. The solution was heated to 70 °C to completely dissolve the oxides, leading to a bright orange solution. (TMSO)I powder (1 mmol) was then added to the solution, causing the immediate precipitation of a polycrystalline powder with the color ranging from orange to deep red upon increasing x. Samples were collected by filtration under vacuum and washed with anhydrous ethanol. Typical yields are ca. 80%.

(TMSO)$_3$Pb$_{3x}$Bi$_{2(1−x)}$Br$_9$ (0 < x < 1). PbO and Bi_2O_3 powders (mmol reported in Table S1) were dissolved in 6 mL of HBr by heating the solution to 70 °C. Consequently, (TMSO)Br powder (1 mmol) was added to the solution, causing the immediate precipitation of a polycrystalline yellow powder. The crystals were collected by filtration under vacuum and washed with anhydrous ethanol. Typical yields are ca. 45%. See Table S2 for the analytical data of all of these species.

Characterization. *XRPD Analysis.* XRPD data were collected at room temperature on a vertical scan $\theta-\theta$ Bruker D8 Advance powder diffractometer equipped with a LynxEye PSD detector in the 3−105° 2θ range, sampling at 0.02° and with a scan time lasting approximately 15 h. Generator settings: 40 kV, 40 mA; fixed divergence slit: 0.5°; goniometer radius: 300 mm; sample holder for a flat specimen Bragg−Brentano parafocusing geometry: zero background silicon monocrystals, with a 0.2 mm deep cavity; Ni-filtered Cu Kα radiation.

Ab Initio Crystal Structure Determination from Laboratory X-ray Diffraction (XRD) Data. The structure determination of the $(TMSO)PbI_3$ crystal phase followed a standard protocol devised in the past by us and others,[30−32] hereafter detailed. Standard peak search methods, followed by profile fitting, allowed the accurate estimate of the low-angle peak position, which, through the SVD indexing algorithm,[33] provided a primitive orthorhombic cell [a = 7.81, b = 11.20, c = 14.40 Å, GOF(20) = 53.4]; all computations were performed using TOPAS-R.[34] Space group determination through the analysis of systematic absences indicated *Pnma* as a probable space group, later confirmed by successful structure solution and refinement.

https://doi.org/10.1021/acs.jpcc.1c02571
J. Phys. Chem. C 2021, 125, 11728−11742

Table 1. Crystal Data for the Four TMSO/Halide End Members, Characterized by XRPD

species	$(TMSO)PbI_3$	$(TMSO)PbBr_3$	$(TMSO)_3Bi_2I_9$	$(TMSO)_3Bi_2Br_9$
formula	$C_3H_9I_3OPbS$	$C_3H_9Br_3OPbS$	$C_9H_{27}Bi_2I_9O_3S_3$	$C_9H_{27}Bi_2Br_9O_3S_3$
fw, g mol^{-1}	681.08	540.08	1839.60	1416.60
system	orthorhombic	orthorhombic	orthorhombic	orthorhombic
space group	*Pnma*	*Pnma*	*Pnma*	*Pnma*
a, Å	7.8157(1)	7.5697(1)	7.4530(1)	7.0351(1)
b, Å	11.1996(1)	10.7768(3),	11.2169(2)	10.6613(1)
c, Å	14.3780(1)	13.9143(3)	14.4009(2)	13.9190(2)
V, Å^3	1260.29(4)	1135.09(5)	1203.92(3)	1043.98(2)
Z	4	4	4/3	4/3
ρ_{calc}, g cm^{-3}	3.590	3.160	3.383	3.004
μ(Cu Kα), cm^{-1}	840.0	417.1	801.9	364.2
(*hkl*), g	(100), 1.48	(100), 0.87	(100), 0.97	(100), 1.24
R_p, R_{wp}	0.064, 0.085	0.040, 0.054	0.060, 0.089	0.029, 0.049
R_{Bragg}	0.064	0.034	0.063	0.047
2θ range, °	9.9−105.0	9.0−105.0	9.0−105.0	9−105.0

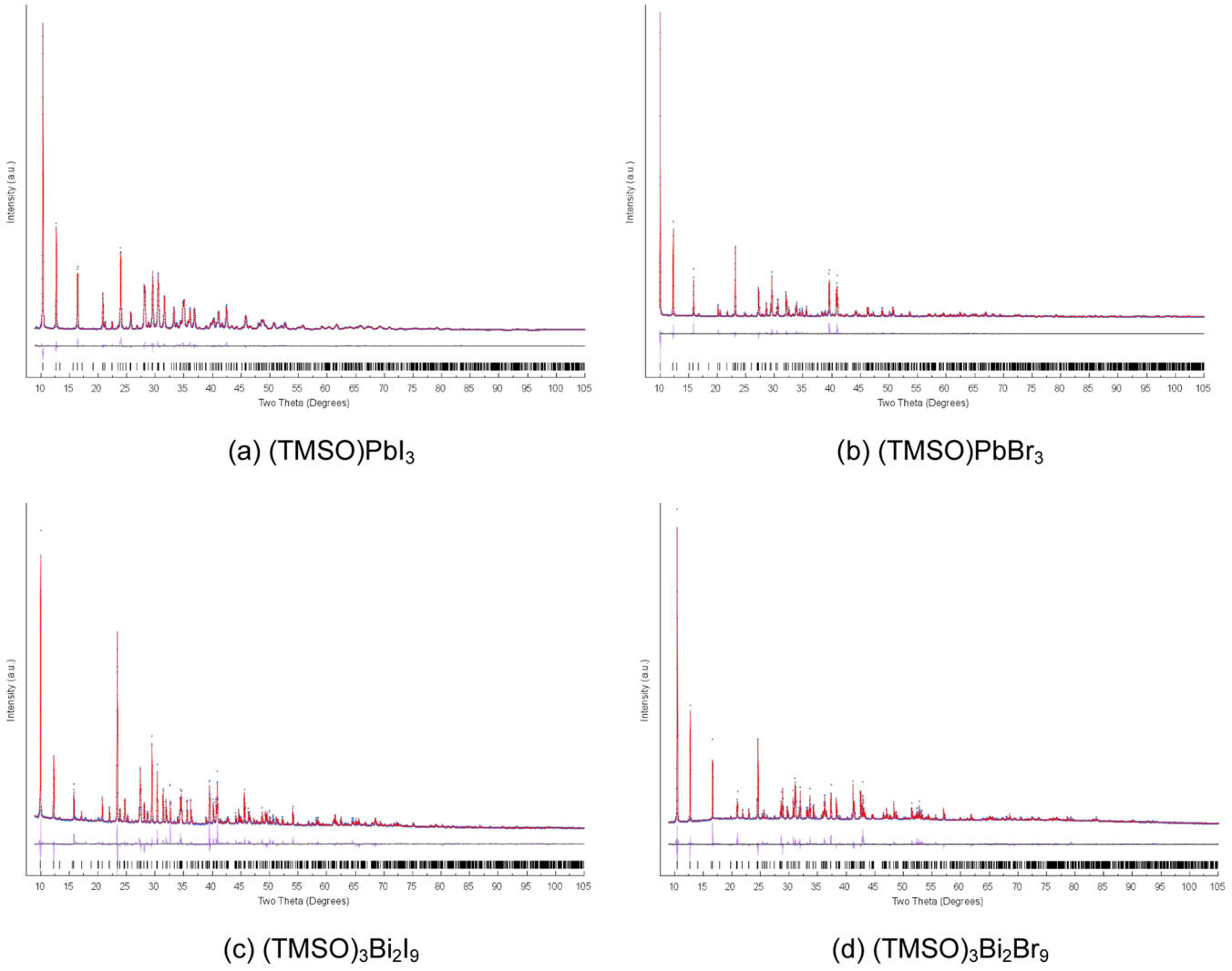

Figure 1. Rietveld refinement plots for: (a) $(TMSO)PbI_3$, (b) $(TMSO)PbBr_3$, (c) $(TMSO)_3Bi_2I_9$, and (d) $(TMSO)_3Bi_2Br_9$. Observed and calculated traces in blue and red, respectively, with the difference plot (in violet) and peak markers (black bars) at the bottom.

Structure solution was performed by the Monte Carlo/simulated annealing technique using freely floating independent atom models for Pb and I atoms and a rigid model described by the Z-matrix formalism with standard geometrical parameters, for the $TMSO^+$ cation, taking care of the presence of a crystallographic mirror plane about which the organic fragment is located (jointly to Pb and to one iodine atom). The final refinements were carried out by the Rietveld method, maintaining the rigid bodies introduced at the structure solution stage. The background was modeled by a polynomial function of

https://doi.org/10.1021/acs.jpcc.1c02571
J. Phys. Chem. C 2021, 125, 11728−11742

the Chebyshev type, peak profiles were described by the fundamental parameters approach[35] and a common (refinable) isotropic thermal factor was attributed to all atoms. The March–Dollase correction for preferred orientation[36] was applied in the form of $g(hkl)$ and is quoted below.

As the $(TMSO)PbBr_3$, $(TMSO)_3Bi_2I_9$, and $(TMSO)_3Bi_2Br_9$ end members were found isomorphous with $(TMSO)PbI_3$, their structural models were taken from this phase, with the caveat of substituting the unique metal atom with a partially vacant (site occupancy factor = 2/3) Bi ion, maintaining sample stoichiometry. Table 1 synoptically collects the crystal data and the pertinent Rietveld refinement agreement factors. Given the metal cation/vacancy disorder discussed below, for the pure $(TMSO)_3Bi_2I_9$ compound, a split Bi-atom model and an anisotropic modeling of its atomic displacement parameters were also tested, which ended up with similar or slightly lower profile agreement factors, R_{wp}'s (8.93 and 8.62%, respectively) than the isotropic/unsplit model (R_{wp} 8.88%, see Table 1). In the anisotropic model, U_{ij}'s provided an imaginary ellipsoid (with a negative U_{33} parameter and, as expected, a large U_{11} contribution). Consequently, we maintained the pristine isotropic description of the (unsplit) Bi atom, also to maintain consistency with the other (Pb-containing) structural models.

Figure 1 shows the final Rietveld refinement plots for $(TMSO)PbI_3$, $(TMSO)PbBr_3$, $(TMSO)_3Bi_2I_9$, and $(TMSO)_3Bi_2Br_9$. Fractional atomic coordinates and crystal structure details were deposited with the CCDC (CSD Codes 2069439–2069442). These data can be obtained free of charge upon request from the Cambridge Crystallographic Data Centre via www.ccdc.cam.ac.uk/data_request/cif.

For the mixed-metal (doped) crystal phases, a completely random distribution of Pb/Bi in their crystallographic site was assumed, justified by the absence of superstructure peaks. Although in some cases (and, in a relevant manner, in the $(TMSO)_3Pb_{0.99}Bi_{1.34}I_9$ and $(TMSO)_3Pb_{1.11}Bi_{1.26}Br_9$ phases), the shape of hkl peaks of the $h \neq 0$ class needed an additional convolution to be fitted, which was performed, wherever possible, using box or Gaussian functions of refinable width. This aspect is further discussed in the following. The final Rietveld refinement plots for the mixed-metal samples are reported in Figures S1–S7. Additional crystal data are summarized in Table S3.

Scanning Electron Microscopy (SEM). SEM images in secondary-electron mode were collected with a FEI Quanta 200 microscope equipped with an EDAX energy-dispersive fluorescence analyzer using a 20 kV electron beam.

Inductively Coupled Plasma Optical Emission Spectroscopy (ICP-OES). A Perkin-Elmer Optima 2100 ICP-OES spectrometer equipped with an autosampler model S10 was used to accurately quantify Bi in the doped samples. WinLab 32 software (Perkin-Elmer) was used for the acquisition and processing of the data. An emission wavelength of 190.171 nm was used for Bi. Calibration curves of Bi^{3+} ions (0.5–5 ppm) were obtained by diluting ICP multielement standard solution VIII (Certipur reference material). For each sample, 10 mg were mineralized in 10 mL of concentrated HNO_3 until half of the volume evaporated. The remaining liquid was recovered quantitatively in a 25 mL graduated flask, then filled with distilled water. To fall within the range of the calibration curve, the resulting solution was either analyzed as prepared or diluted up to 1:20 with aqueous HNO_3. The stoichiometry, expressed as the molar fraction of Pb, is reported with two significant digits for simplicity, although Bi concentration measurements are accurate to the 10^{-3} level.

Thermal Analyses (Thermogravimetric (TG) and Differential Scanning Calorimetry (DSC)). Thermogravimetric (TG) and differential scanning calorimetry (DSC) curves were acquired simultaneously from 20 to 900 °C using a Netzsch STA 409 PC/PG thermal analyzer. The samples were heated in alumina crucibles at a heating rate of 10 °C·min^{-1} under a 20 mL·min^{-1} N_2 flow. TG/DSC data were analyzed by Proteus software (Netzsch).

X-ray Fluorescence Spectroscopy (XRF). Gently ground powders of the seven mixed-metal phases were deposited on a polycarbonate film and analyzed with a MiniPal2 XRF spectrometer (PANalytical), working with a Cr-anode at 30 kV and 3 μA, using a Ag filter. X-ray fluorescence lines were measured for Pb (L_α and L_β lines, at 10.5 and 12.6 keV, respectively) and Bi (L_α and L_β lines, at 10.8 and 13.0 keV, respectively). Intensity calibration was performed using an equimolar amount of Pb and Bi, using a $(TMSO)PbI_3$ and $(TMSO)_3Bi_2I_9$ mixture. Complete agreement of the doped sample compositions obtained from XRF and ICP-OES was obtained, as shown in Figure S8 in the Supporting Information.

Diffuse Reflectance Spectroscopy. UV–vis-NIR reflectance spectra of the powders were measured in the 200–800 nm range using a UV-2600 Shimadzu spectrometer. $BaSO_4$ was used as the nonabsorbing reflectance reference. The Kubelka–Munk function $F[R]$ was calculated from the reflectance spectrum, using the $F[R] = (1 - R)^2/2R$ relationship. Taking $F[R]$ as the representative of the sample absorbance spectrum, extrapolation of the linear portion of the $(F[R]\ h\nu)^2$ vs $h\nu$ plot on the $h\nu$ axis provided experimentally accessible direct band gap values (Tauc plots).

DFT Simulations. Periodic ab initio quantum mechanical calculations were carried out with density functional theory (DFT) using the PWscf package in the Quantum Espresso suite.[37−39] Kohn–Sham equations are solved with the generalized gradient approximation (GGA),[40] adopting the PBE exchange-correlation functional[41] within the projector augmented wave (PAW) method.[42] The cell and the atomic relaxations were carried out using a centered 2 × 1 × 1 Monkhorst–Pack (MP) grid with a plane wave cutoff of 40 Ry for the $(TMSO)PbX_3$ samples. In the case of $(TMSO)_3Bi_2X_9$, the calculations were performed on a 3 × 1 × 1 supercell, which contains 12 pseudo-perovskite B sites containing 8 Bi and 4 vacancies. For these supercells, the structure optimization was carried out on the Γ point with a 50 Ry cutoff. Preliminary testing on variable-cell relaxation of the $(TMSO)PbI_3$ structure led to the choice of the PBE functional to describe these systems (Table S4), and dispersion forces were added into the description of our samples to achieve for all of the end members a discrepancy in the volume less than 7%. The electronic structure calculations were performed to account for spin–orbit coupling (SOC) and with a denser MP grid: 8 × 4 × 4 and 2 × 4 × 4 for $TMSOPbX_3$ and $(TMSO)_3Bi_2X_9$, respectively. For all calculations, a convergence threshold of 10^{-6} au was used.

RESULTS AND DISCUSSION

Synthesis and Stoichiometry. The samples were synthesized using a simple one-pot method: the desired amount of Pb and Bi precursors was dissolved in a hot HX solution. The addition of the (TMSO)X salt causes precipitation of the pseudo-perovskite. This method leads to highly pure polycrystalline samples (Figure 1), with crystallites of different sizes

https://doi.org/10.1021/acs.jpcc.1c02571
J. Phys. Chem. C 2021, 125, 11728–11742

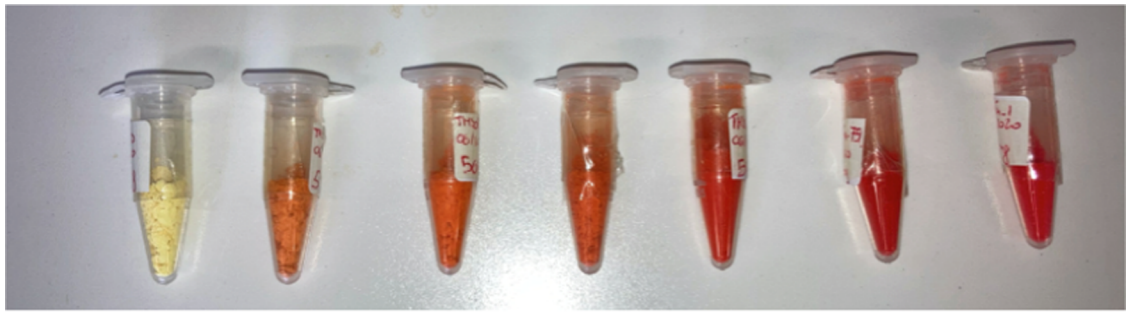

(a)

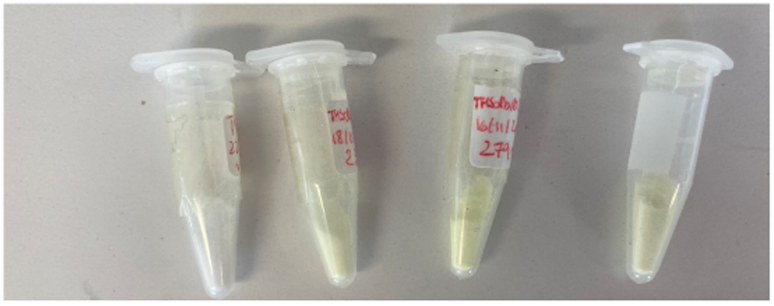

(b)

Figure 2. (a) Powders of $(TMSO)PbI_3$, $(TMSO)_3Pb_{3x}Bi_{2(1-x)}I_9$ (x = 0.98, 0.92, 0.89, 0.56, and 0.33), and $(TMSO)_3Bi_2I_9$, left to right and (b) powders of $(TMSO)PbBr_3$, $(TMSO)_3Pb_{3x}Bi_{2(1-x)}Br_9$ (x = 0.83 and 0.37), and $(TMSO)_3Bi_2Br_9$, left to right.

depending on the speed of the precipitation reaction. In all cases, polycrystalline samples with different grain sizes and dispersity were obtained. In particular, the end-member samples are composed of prismatic crystallites around 5−20 μm, while the doped samples also show a small fraction of elongated crystals with increasing Bi content together with larger prismatic crystals (Figure S9).

Room temperature syntheses, or even preparations in moderately warm solvents, of 3D hybrid lead halide perovskite are known to produce defective species, which possess a variety of defects (vacancies, dislocations, and twin boundaries, to mention a few),[43−45] which heavily impact on their excellent photophysical performances. In the present case, where many "metal" vacant sites are present (up to 33% in the $(TMSO)_3Bi_2I_9$ species), their presence numerically overwhelms those which are serendipitously, randomly, or occasionally formed by kinetic, and not thermodynamic, control during synthesis. Thus, even if present, this latter kind of defectiveness is considered marginal and of the second order with respect to the primary one, and is neglected here.

It is noteworthy that the overall yields of iodide-based powders were significantly higher (by a factor of ca. 1.5) than those observed when bromide was employed. Figure 2 clearly shows the effect of Bi concentration on the color of the powders obtained, hinting at a very substantial impact of the Bi dopant on the electronic structure near the band gap.

The Bi substitution into $(TMSO)PbI_3$ can be described with the quasi-chemical equation in the Kröger−Vink notation

$$3Pb_{Pb}^{x} + 2BiI_3 \rightarrow 2Bi_{Pb}^{\bullet} + V_{Pb}'' + 3PbI_2$$

On average, three Pb atoms are substituted by two Bi atoms, and vacant cation sites (V_{Pb}'') are also generated. Accordingly, the solid solutions are best described by the following formula

$$(TMSO)_3Pb_{3x}Bi_{2(1-x)}X_9 \quad (0 < x < 1)$$

For x = 1 and x = 0, this leads to the all-lead (Pb_3) and all-bismuth (Bi_2) end-member composition, respectively.

Other possible charge compensation mechanisms (e.g., $TMSO^+$ vacancies)[46,47] are ruled out by XRD analysis and stereochemical considerations. Indeed, the absence of a significant amount of $TMSO^+$ cations in the entire crystal framework would generate large enough voids (estimated by Hofmann rules[48] to approach 136 Å^3, compatible with a sphere of ca. 6.4 Å diameter), prone to framework collapse, not being sustained by 3D connectivity as in conventional perovskites or, alternatively, in the ubiquitous MOF realm. TG and DSC measurements of these samples showed thermal stability up to 200 °C with no phase transitions in the 25−200 °C temperature range. This finding is of relevance if compared to classical perovskite structures, which have rather complex phase diagrams.[49−51]

The stoichiometries of the four end-member species are easily deduced from TG curves (Figures S11 and S12) since the weight losses, by release of (TMSO)X, are entirely resolved for the $(TMSO)X−PbX_2$ and $(TMSO)X−BiX_3$ materials. Pb-containing samples follow a 1:1 (TMSO/Pb) ratio, while the Bi-based ones are consistent with a 3:2 (TMSO/Bi) ratio, leading to the $(TMSO)PbX_3$ and $(TMSO)_3Bi_2X_9$ formulae, respectively, further confirmed by XRPD. These stoichiometries are consistent with those of other hybrid halide pseudo-perovskites based on these B-site cations.[52] TG curves of mixed-metal samples show that their decomposition occurs through two overlapping events (attributed to PbX_2 and BiX_3 weight losses), resulting in a slight underestimation of the Bi content of the investigated samples. ICP-OES was therefore used to determine the stoichiometry of the five I-based and the two Br-based mixed-metal samples accurately. The obtained compositions are reported in Table 2, expressed as the Bi fraction [%Bi = atomic percentage of Bi ions over the total of B-site cations − (Bi + Pb)], together with the $(TMSO)_3Pb_{3x}Bi_{2(1-x)}X_9$ formula.

https://doi.org/10.1021/acs.jpcc.1c02571
J. Phys. Chem. C 2021, 125, 11728−11742

Table 2. Bi-Doping Level, or %Bi [the 100 × Bi/(Pb + Bi) Ratio], Derived from ICP-OES Analysis and Stoichiometry for the Solid Solutions with the Formula $(TMSO)_3Pb_{3x}Bi_{2(1-x)}X_9$

stoichiometric formula	%Bi	x
$(TMSO)_3Pb_{2.94}Bi_{0.04}I_9$	1	0.98
$(TMSO)_3Pb_{2.76}Bi_{0.16}I_9$	5	0.92
$(TMSO)_3Pb_{2.67}Bi_{0.22}I_9$	8	0.89
$(TMSO)_3Pb_{1.68}Bi_{0.88}I_9$	34	0.56
$(TMSO)_3Pb_{0.99}Bi_{1.34}I_9$	58	0.33
$(TMSO)_3Pb_{2.49}Bi_{0.34}Br_9$	12	0.83
$(TMSO)_3Pb_{1.11}Bi_{1.26}Br_9$	53	0.37

Theoretical and experimental (TG and ICP-OES) x values with %Bi and yields for the different syntheses are reported in Table S2.

Crystallochemical Analysis. *End Members.* The four end members are isomorphous crystal phases sharing the orthorhombic *Pnma* space group. The Pb-based structures contain infinite polyanionic one-dimensional chains with the formula $[PbX_3]_\infty$, built by face-sharing $[PbX_6]$ octahedra running parallel to the *a* axis; the organic cations are placed between these chains. The crystal packing diagram for the $(TMSO)PbI_3$ species is shown in Figure 3. At the drawing resolution, the

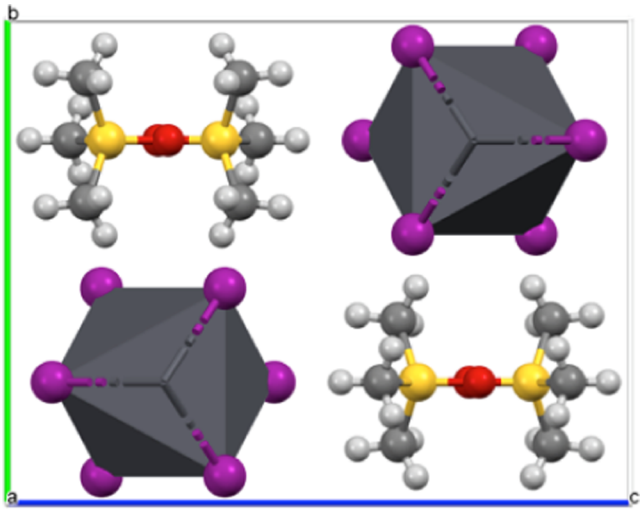

Figure 3. Schematic drawing of the crystal packing of $(TMSO)PbI_3$, highlighting the octahedral coordination of Pb^{2+} cations by iodide anions (in violet) and viewed down the direction of propagation of the infinite $([PbI_3]^-)_\infty$ polyanions, [100]. C, S, O, and H atoms in gray, yellow, red, and white, respectively.

$(TMSO)PbBr_3$ analogue is almost identical, except for slightly smaller lattice parameters and, therefore, is not shown here. Table 3 synoptically collects the most relevant structural parameters for these two Pb-based species and the other Bi-based ones discussed later in this section.

In the $(TMSO)PbI_3$ and $(TMSO)PbBr_3$ phases, the polyanionic lead halide chains are topologically identical; they exhibit small differences due to the different sizes of the iodide and bromide ions (2.06 and 1.82 Å crystal radii, respectively[53]), resulting in average bond lengths of 3.24 Å (Pb−I) and 3.11 Å (Pb−Br), respectively. Thanks to the shortening of the Pb−Br distances, and the relative constancy of the Pb−X−Pb angles (average values in $(TMSO)PbX_3$: 74.0° for X = I vs 75.1° for Br), the interionic (nonbonding) Pb···Pb distance along the 1D chain in $(TMSO)PbBr_3$ (3.79 Å) is shorter by ∼3% than in the $(TMSO)PbI_3$ crystal phase (3.91 Å). Both values are significantly smaller (by more than 0.10 Å) than those found in the (protonated) proton sponge analogues ($(C_{14}H_{19}N_2)$-PbX_3, X = I, Br)[54] and speak for the additional noninnocent character of the cation/polyanion interaction in the crystal and for the partial flexibility of the polyhalide chains upon I or Br occurrence.

In the isomorphous $(TMSO)_3Bi_2I_9$ and $(TMSO)_3Bi_2Br_9$ crystal phases, an ordered sequence of $[Bi_2I_9]^{3-}$ ions, separated by a vacant site, is present along the *a* axis. A comparison of the two fully ordered chains, where metal sites are 100% populated [as in $(TMSO)PbX_3$] or alternate with vacancies in a 2:1 ratio [as in $(TMSO)_3Bi_2X_9$], is shown in Figure 4. The absence of X-ray superstructure peaks with fractional *h* indices clearly demonstrates that no crosstalking among parallel chains in the Bi species is at work, as it is expected from the relatively long intermetallic distances connecting ions from different chains (or dimers) well separated in the *bc* plane. This finding forces the entire crystallographic description to be discussed within an average space group with a short(er) *a* axis, rather than an ordered sequence that would require a (at least) 3× longer *a* axis value to cope with both the Bi/Bi/V and TMSO periodicities. The necessary occurrence of diffuse scattering, falling below and between Bragg peaks, was not observed, as, being much weaker than reflection intensities, cannot be easily determined by XRPD laboratory data. As a direct consequence of this description, the real bond distances are different from those obtained by the translational averaging and cannot be therefore directly compared with values for isolated $[Bi_2I_9]^{3-}$ and $[Bi_2Br_9]^{3-}$ species retrieved from the CSD (see the "CSD" columns of Table 3).

The existence of similar species is found in the scientific literature, where $TMSO^+$, or even the triethylammonium cations, Et_3NH^+, give rise to a similar crystal packing in *Pnma*: $(Et_3NH)MnCl_3$,[55] $(Et_3NH)CdCl_3$,[56] $(TMSO)CdCl_3$,[57] $(TMSO)CdBr_3$,[57] and their solid solutions $(TMSO)Cd(Cl,Br)_3$.[58] In contrast, the absence of systems in the CSD where $[Bi_2X_9]^{3-}$ moieties are linearly juxtaposed in the crystal through a small gap (a vacant site V''_{Pb}) (while maintaining structural coherence along 1 crystal periodicity) does not enable to inspect the effect of the missing atom on the axial length from parallel cases. To this goal, taking values from Table 3, a simple geometrical approach can be envisaged: (i) given that, for $(TMSO)PbI_3$, the shortest Pb···Pb distance is 3.91 Å, and the head-to-tail Pb···Pb···Pb···Pb separation of a linear Pb_4 quartet is 3 times larger (11.73 Å); (ii) the analogous separation in $(TMSO)_3Bi_2I_9$ (i.e., Bi···Bi···V···Bi) appears to be 3 × 3.73 = 11.19 Å only; and (iii) taking the Bi···Bi distance within known, isolated, $[Bi_2I_9]^{3-}$ fragments from the CSD database (average value = 4.19 Å), each Bi···V value can be estimated to be close to (11.19−4.19)/2 = 3.50 Å. This aspect is discussed in the following section, dealing with the simultaneous presence of Pb and Bi ions and the stoichiometrically related abundancy of vacant sites.

Pb−Bi Solid Solutions. The mixed-metal phases, prepared by combining Bi^{3+} and Pb^{2+} in various molar ratios, are structurally isomorphous with the parent compounds. Their XRPD traces (see Figure 5a) show minor and predictable variations in the peak position and intensity upon changing the stoichiometry of the material. For all of the $(TMSO)_3Pb_{3x}Bi_{2(1-x)}I_9$ species investigated here, the derived

https://doi.org/10.1021/acs.jpcc.1c02571
J. Phys. Chem. C 2021, 125, 11728−11742

Table 3. Synoptic Collection of Relevant (Room Temperature) Structural Parameters for the Crystal Structures Reported in This Article[d]

parameter	$(TMSO)PbI_3$	$(TMSO)PbBr_3$	$(TMSO)_3Bi_2I_9$	CSD (Bi_2I_9)	$(TMSO)_3Bi_2Br_9$	CSD (Bi_2Br_9)
B···B, Å	3.91	3.79	3.73	4.19(7)	3.52	3.99(4)
B···X1, Å	3.19; 3.26	3.08; 3.11	3.00; 3.06		2.81; 2.86	
B···X2, Å	3.23; 3.27	3.10; 3.13	3.17; 3.22		2.96; 2.99	
<B···X> and spread, Å	3.24; 0.03[b]	3.11; 0.02[b]	3.14; 0.09[b]	2.96(3)[c]	2.93, 0.08[b]	2.73(3)[c]
				3.24(6)[c]		3.03(4)[c]
B···Xn···B, °	X1: 74.5	X1: 75.5	75.9		X1: 76.8	
	X2: 73.8	X2: 74.9	71.3		X2: 72.5	
<B···X···B> and spread, °	74.0; 0.4[b]	75.1; 0.3[b]	72.8; 2.6[b]	80.5(1.5)	73.9; 2.5	82.3(1.1)

[a]Statistically derived e.s.d's from XRPD data are <0.02 Å for Pb−X bond distances and ∼0.3° for Pb−X−Pb angles. [b]Italicized values for the spread of the B−X distances and B−X−B angles are discussed in the text. [c]CSD-retrieved average bond distances and spread for terminal and μ_2-bridging halides, respectively, in isolated Bi_2X_9 fragments. [d]B = Pb or Bi.

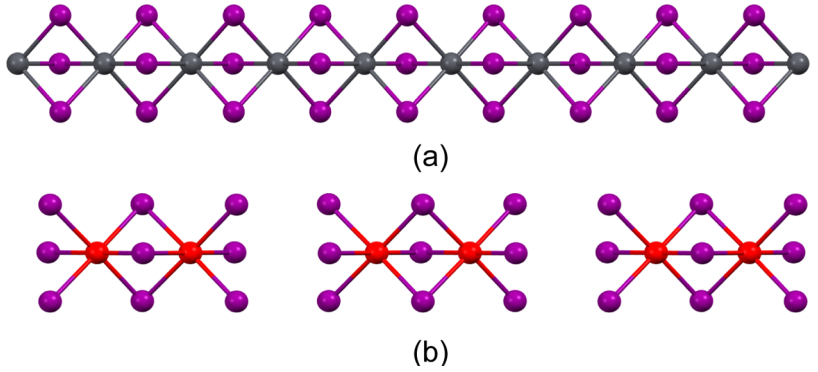

Figure 4. Atomic disposition along the *a* axis of: (a) 1D chains with 100% Pb^{2+} ion occupancy in the infinite $([PbI_3]^-)_\infty$ polyanion and (b) isolated $[Bi_2I_9]^{3-}$ trianions, separated by vacant B sites. Pb in gray, Bi in red, and I in violet.

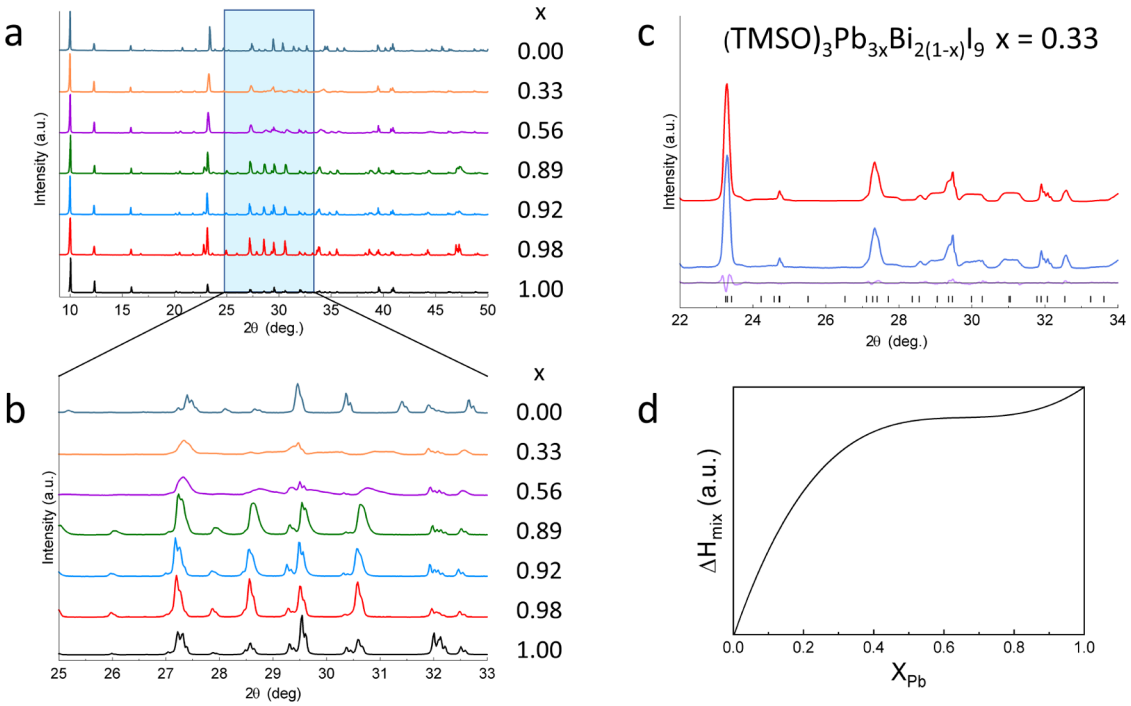

Figure 5. (a) Comparison of the raw diffraction data of $(TMSO)PbI_3$, the doped $(TMSO)_3Pb_{3x}Bi_{2(1-x)}I_9$ ($0 < x < 1$), and the $(TMSO)_3Bi_2I_9$ crystal phases in the 7−50° 2θ range (bottom to top); (b) magnification of the 25−33° section, where the peak shape anomaly discussed in the text is more evident; (c) fit of the 22−34° region for the $(TMSO)_3Pb_{0.99}Bi_{1.34}I_9$ sample, where sharp peaks correspond to $0kl$ reflections, while "trapezoidal" regions belong to $h \neq 0$ ones. This phenomenological description, obtained by selective convolution of a rectangular function of unit area with a width proportional to h^2, is physically interpreted in the Results and Discussion section. Observed data: blue dots; calculated trace: red lines; and difference plot and peak markers at the bottom; and (d) relative enthalpy of mixing of the solid solutions as a function of Pb molar fraction (X_{Pb}).

https://doi.org/10.1021/acs.jpcc.1c02571
J. Phys. Chem. C 2021, 125, 11728−11742

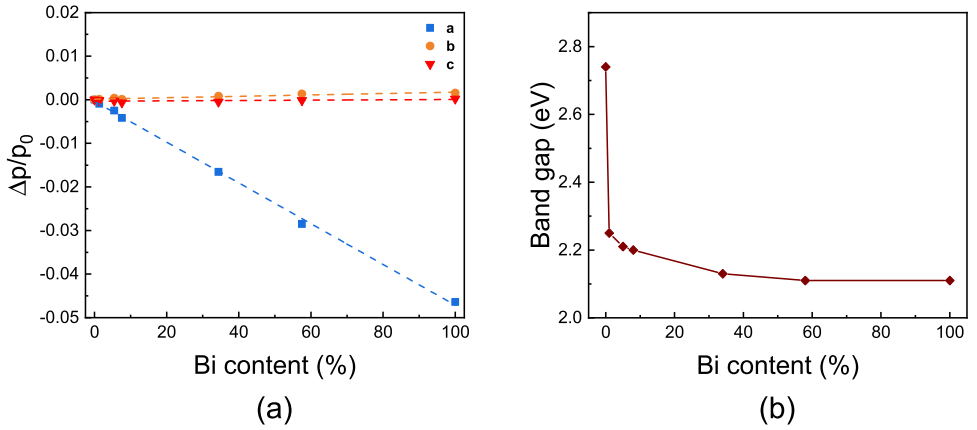

Figure 6. (a) Lattice parameter relative variation vs %Bi [Bi content (%)], in the form of $\Delta p/p_0$ (where $p = a, b, c$, and p_0 values are taken with reference to the $(TMSO)PbI_3$ species, that with $x = 0$) for the $(TMSO)_3Pb_{3x}Bi_{2(1-x)}I_9$ series. (b) Optical band gap vs %Bi.

unit cell parameters (see Table S3) follow distinct trends as a function of Bi/Pb ratio. In particular, the *b* and *c* parameters (normal to the metal halide chains) are basically unaffected by the extent of the substitution; the *a* parameter, on the contrary, decreases linearly with increasing Bi content (%Bi), as defined above (see Figure 6). This observation is in line with the nearly constant *b* and *c* parameters (cross section of the polyanionic metal iodide chains), while the relative size of ions and the presence of vacant sites shrink the average periodicity in *a*.

Panel (b) of Figure 5 shows the XRD peak shapes of the crystal phases of the intermediate composition in detail. Those with $x = 0.56$ ($n = 4$) and $x = 0.33$ ($n = 5$) are of particular interest since a significant broadening is observed for *hkl* peaks having $h \neq 0$, while 0*kl* peaks, not affected by ordering or disordering within the Pb/Bi/V chains, retain their sharp lineshape.

The odd appearance of trapezoidal (flat-top) peaks under these circumstances (see Figure S13) speaks for a uniform spread of "cell lengths" within a wide (a_{min}, a_{max}) range, rather than a purely statistical distribution (generating smooth Gaussian or binomial distribution-related shapes). Accordingly, the refinement was tackled using a convolution with a rectangular function of unit area [$\mathrm{rect}(2\theta) = 1/D$ (for $|2\theta| < D/2$) and $\mathrm{rect}(2\theta) = 0$, elsewhere, with $D = mh^2$ ($m > 0$, refinable)] providing a maximum *D* value of $0.144h^2$ in the most broadened case (Figure 5c). In search for the physical meaning of a uniform distribution of unit cells, or of interatomic separations along **a** between Pb, Bi, and vacant sites, we propose that these mixed-metal phases are somewhat reminiscent of 1D disordered binary systems (A_xB_{1-x}), which occasionally display a shallow (nearly flat) ΔG_{mix} curve for a wide range of *x* values, resulting in equiprobable configurations in real space.[59] In our case, the analysis of the thermodynamics of the mixing of the (Pb, Bi, V) species in the cation sites suggests that a similar situation may occur at intermediate *x* values. A complete derivation of the pertinent equations on which the following considerations are grounded is reported in the Supporting Information, separately treating enthalpic and entropic contributions for the stoichiometrically constrained Pb, Bi, and V molar fractions.

The theoretical ΔH_{mix} curve as a function of *x* for the Pb/Bi samples (based on the regular solution model) is highly asymmetric and with very low values for $x < 1/3$ (see Figure 5d). This latter situation describes a relatively ordered system with strongly interacting Bi ions and vacancies (i.e., V's lie in the proximity of Bi^{3+} ions). In the $1/3 < x < 2/3$ range, the ΔH_{mix} curve is relatively shallow and reaches zero for $x = 1$. Negligible ΔH_{mix} values correspond to an ideal solution, where dilute noninteracting Bi and V defects do not affect the Pb-rich lattice.

Therefore, in the Bi-rich regime (low *x* values), a strong tendency toward highly correlated Bi^{3+}/V/B sequences within the chains exists (B = Pb^{2+} or Bi^{3+}), overcoming alternative configurations resulting in V−V pairs. These are energetically unfavored (say, impossible) since uncoordinated halides between two vacant cationic sites would result therefrom. At the other end of the phase diagram, in the Pb-rich regime (large *x* values), the arrangement of cations and vacancies is essentially random, resembling more of an ideal solid solution (in line with the more regular peak shape in the XRD patterns). In the vast intermediate *x* value region two opposite tendencies are at work: (i) the ΔH-favored ordering and (ii) the ΔS-induced randomization of ion/vacancy configurations.

As one moves to the low *x* regime, where a higher Bi and V content is present and Bi/V positioning is heavily correlated, the huge negative enthalpy contribution dominates the ΔG_{mix}. Following the algebraic analysis provided in the Supporting Information, the $(TMSO)_3Pb_{0.99}Bi_{1.34}I_9$ sample with $x = 0.33$ lies at the maximum value of ΔS_{mix} (the minimum of $-T\Delta S_{mix}$) and is highly stabilized on entropic grounds. If cations were to be placed freely in a random chain, the V−V pairs of this sample would occur with a non-negligible 11% probability. Given that V−V pairs are highly enthalpically unfavored, a nonrandom arrangement of atoms must be adopted, with an enforced and crucial short-range ordering.

In a simplified picture, the disordered chain mixed-metal structures can be explained as an assortment of Pb/Pb/Pb and Bi/V/Bi genes, each having identical charge and similar, but not equal, length. In such a solid solution, the entropic and enthalpic contributions countercorrelate (hence, the flat ΔG_{mix} curve), and each chain would be better represented by short (compositionally homogeneous) segments alternating along **a**, with variable levels of segregation, as it occurs in random block copolymers and poloxamers.[60] Further work is necessary to obtain a quantitative modeling of the XRD pattern of the mixed Pb/Bi phases using a stochastic disorder model previously developed for close-packed metals[61] to correctly reproduce the anisotropic broadening reflections with $h \neq 0$.

An alternative hypothesis might be, however, put forward: if the solubility of the Bi and Pb parent compounds is different and, for example, Bi-rich crystals precipitate first, then Bi-ion

https://doi.org/10.1021/acs.jpcc.1c02571
J. Phys. Chem. C 2021, 125, 11728−11742

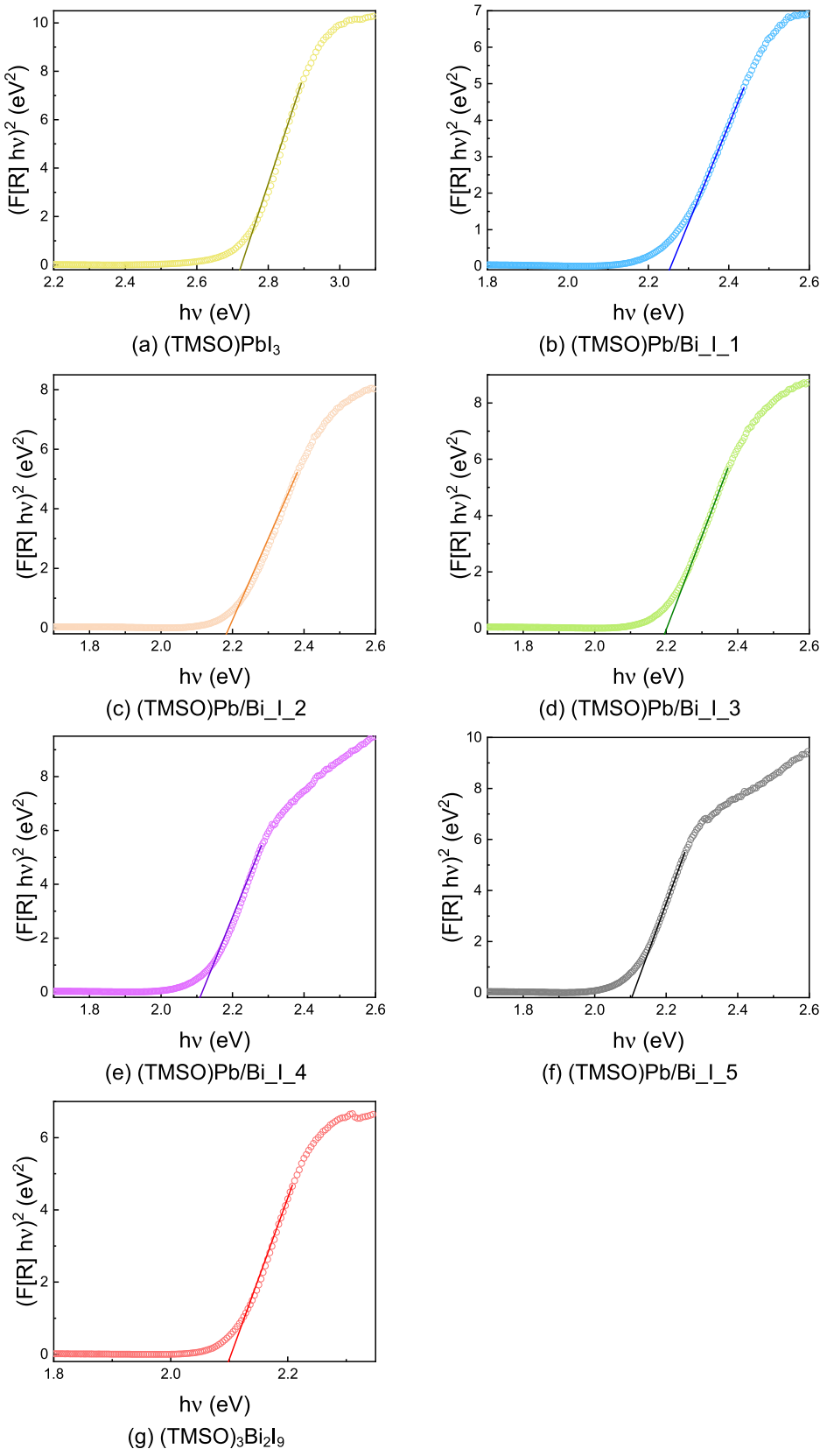

Figure 7. Tauc Plots of (a) $(TMSO)PbI_3$, (b–f) $(TMSO)_3Pb_{3x}Bi_{2(1-x)}I_9$ ($0 < x < 1$), and (g) $(TMSO)_3Bi_2I_9$.

depletion in solution may induce the progressive crystallization of Pb-rich(er) species, resulting in a continuous distribution of compositions and lattice parameters (hence, the trapezoidal XRPD peak shapes). This appealing hypothesis, which could be in principle tested with a fractional crystallization, could not be proved, as precipitation of our polycrystalline material is very fast (say, immediate), and, accordingly, should not favor this process.

https://doi.org/10.1021/acs.jpcc.1c02571
J. Phys. Chem. C 2021, 125, 11728−11742

Thermal Properties. All of the prepared samples were subjected to thermogravimetric and differential calorimetric analyses (shown in Figures S11 and S12). The iodine-based end members, $(TMSO)PbI_3$ and $(TMSO)_3Bi_2I_9$, showed similar decomposition temperatures (slightly below 200 °C, ΔH = 133 and 56 kJ mol^{-1}, respectively), releasing (TMSO)I and leaving PbI_2 or BiI_3, respectively, with experimental (theoretical) mass losses of 32.4 (32.3) and 35.5 (35.9) %. However, upon increasing the temperature, two very distinct behaviors are found: solid PbI_2 melts at ca. 410 °C, in agreement with literature data,[62] and evaporates appreciably only above 500 °C. The observed enthalpy of fusion (ΔH_{fus} = +17.9 kJ mol^{-1}) appears to be somewhat smaller than that reported in[63] (ΔH_{fus} = +23.3 kJ mol^{-1}). It may result from the formation of nanosized domains or even polytypic stacking of PbI_2 layers disrupting ideal periodicity.[64] At variance, BiI_3, known to sublime at much lower temperatures, shows a progressive sample elimination that is complete at 400 °C.

As expected, the Pb-rich mixed-metal phases ($(TMSO)_3Pb_{3x}Bi_{2(1-x)}I_9$ with x = 0.89−0.98) behave very similar to $(TMSO)PbI_3$ but display a progressively increasing thermal event (broad endotherm and a few percent weight loss below 400 °C, below the melting of PbI_2), attributed to BiI_3 elimination. For the remaining (Bi-rich) mixed-metal crystal phases, while the loss of BiI_3 is easily observed, the sharp endotherm associated with the melting of PbI_2 is missing, as if this material formed in an amorphous or nanocrystalline form (with no well-defined melting point). However, the progressive weight loss, completed slightly above 600 °C, is a clear manifestation of its presence.

Altogether, these sets of coherent data manifest the nonmiscibility of the PbI_2/BiI_3 phases: indeed, neither crystalline $(Pb_xBi_{1-x})I_{3-x}$ phases are known (though possibly present in a complex, poorly characterized, polyphasic mixture)[65] nor the few published phase diagrams of this binary system are conclusive in this regard.[65−67]

Similar considerations can be drawn for the Pb/Bi bromide series. End members $(TMSO)PbBr_3$ and $(TMSO)_3Bi_2Br_9$, beyond (TMSO)Br elimination occurring at ca. 220 °C, clearly show a weak endotherm (melting of $PbBr_2$ near 350 °C, slightly lower than 360 °C,[68] possibly because of the formation of nanosized crystals) and progressive $BiBr_3$ sublimation, respectively. Above 220 °C, mixed-metal phases did not show the endotherm associated with $PbBr_2$ melting, but only a continuous weight loss, terminating at ca. 700 °C. Consistently, the presence of different inflection points indirectly indicates the relative amount of Pb and Bi bromides. It is noteworthy that also in this case $(Pb_xBi_{1-x})Br_{3-x}$ phases are not known. However, a heavily disordered and twinned crystal phase, the ternary $(Bi_9)_4[Bi_3Pb_9Br_{47}]$ sub-bromide, crystallized from a melt of bismuth, lead, and $BiBr_3$, was reported,[69] but, in this context, as it contains "metal-like" Bi_9^{5+} clusters, it is not further discussed.

Optical Properties. The optical band gap (E_g) values were experimentally obtained from Tauc plots, summarized in Figure 7 for the $(TMSO)_3Pb_{3-x}Bi_{2(1-x)}I_9$ series, and in the Supporting Information for the $(TMSO)_3Pb_{3x}Bi_{2(1-x)}Br_9$ series (Figure S14), and collectively reported in Table 4. These plots are calculated from the Kubelka−Munk function assuming direct band gap transitions (see the Methods section). A first inspection of these values reveals a general tendency for both series of crystal phases: as the relative amounts of Bi rise, the band gap decreases. These observations parallel those previously reported on Bi-substituted 3D lead halide perovskites of the general $APb_{1-x}Bi_xX_3$ formula (A = Cs and methylammonium, X = Br and I[70−73]) and on the (still debated) PbI_2/BiI_3 solid solutions.[65] Besides, it is evident that the substitution of a small fraction of Pb by Bi on the all-lead end members is enough to trigger a substantial reduction in the value of E_g: see, for instance, the decrease from 2.74 to 2.25 eV when moving from $(TMSO)PbI_3$ to $(TMSO)_3Pb_{2.94}Bi_{0.04}I_9$ (Bi = 1%). However, beyond that point, the band gap's lowering as a Bi/Pb ratio function is much less remarkable. A similar trend is observed in the bromide-based series as well.

Table 4. Band Gap Values (E_g) from Optical Reflectance Measurements, Along With the Composition

samples	x	E_g (eV)
$(TMSO)PbI_3$	1	2.74
$(TMSO)_3Pb_{2.94}Bi_{0.04}I_9$	0.98	2.25
$(TMSO)_3Pb_{2.76}Bi_{0.16}I_9$	0.92	2.20
$(TMSO)_3Pb_{2.67}Bi_{0.22}I_9$	0.89	2.20
$(TMSO)_3Pb_{1.68}Bi_{0.88}I_9$	0.56	2.13
$(TMSO)_3Pb_{0.99}Bi_{1.34}I_9$	0.33	2.11
$(TMSO)_3Bi_2I_9$	0	2.11
$(TMSO)PbBr_3$	1	3.32
$(TMSO)_3Pb_{2.49}Bi_{0.34}Br_9$	0.83	2.82
$(TMSO)_3Pb_{1.11}Bi_{1.26}Br_9$	0.37	2.79
$(TMSO)_3Bi_2Br_9$	0	2.80

First-Principles DFT Calculations. Ab initio DFT calculations were performed to rationalize the different trends of the electronic properties in the samples. The supercell used to describe the defect structure $(TMSO)_3Bi_2X_9$ is reported in Figure 8, while the optimized lattice parameters are listed in Table 5. For $(TMSO)PbX_3$, the optimized structures show a contraction of the lattice parameters (and volume) with respect to the experimental results. On the contrary, for $(TMSO)_3Bi_2X_9$, the volume of the optimized structures is larger than measured. The relative error on the volume is around 6% for all structures. To better compare the experimental and the calculated structures, the direct band gaps were also calculated. The band structures in Figure 9 show a direct gap typical of a wide band gap semiconductor. Indeed, the bands are relatively flat, which is in line with 1D and 0D pseudo-perovskite structures. Considering the heavy atoms in the structure, for $(TMSO)PbI_3$ and $(TMSO)_3Bi_2I_9$, the influence of the spin−orbit coupling on the band gap values was also tested (Table 6). While the SOC is not needed to reach a good quantitative agreement with the

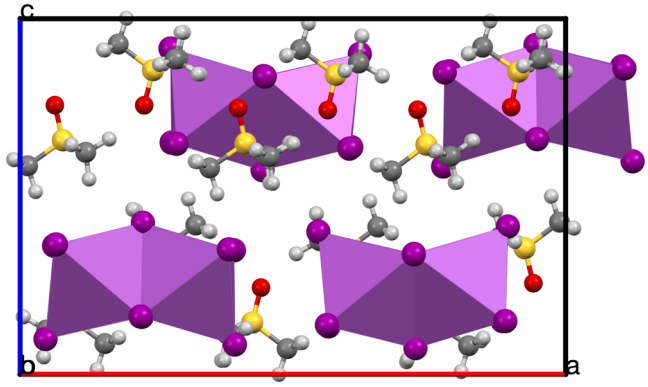

Figure 8. $(TMSO)_3Bi_2I_9$ supercell used in DFT calculations. Colors as in Figure 4.

https://doi.org/10.1021/acs.jpcc.1c02571
J. Phys. Chem. C 2021, 125, 11728−11742

Table 5. Lattice Parameters of the Experimental (Exp) and DFT Optimized (Calc) Structures of the End Members; err% Is Calculated as 100 × $(p_{calc} - p_{exp})/p_{exp}$ (p = a, b, c, V)

		a (Å)	err%	b (Å)	err%	c (Å)	err%	V (Å^3)	err%
$(TMSO)PbI_3$	exp	7.8157		11.1996		14.378		1260.29	
	calc	7.7243	−1.17	11.0278	−1.53	14.0110	−2.55	1193.49	−5.30
$(TMSO)PbBr_3$	exp	7.5697		10.7768		13.9143		1135.10	
	calc	7.4366	−1.76	10.5566	−2.04	13.5324	−2.74	1062.36	−6.41
$(TMSO)_3Bi_2I_9$	exp	22.3590		11.2169		14.4009		3611.77	
	calc	22.2356	−0.55	11.4866	2.40	14.4513	0.35	3691.04	2.19
$(TMSO)_3Bi_2Br_9$	exp	21.1055		10.6613		13.9190		3131.94	
	calc	21.5843	2.27	10.9250	2.47	13.9057	−0.10	3279.10	4.70

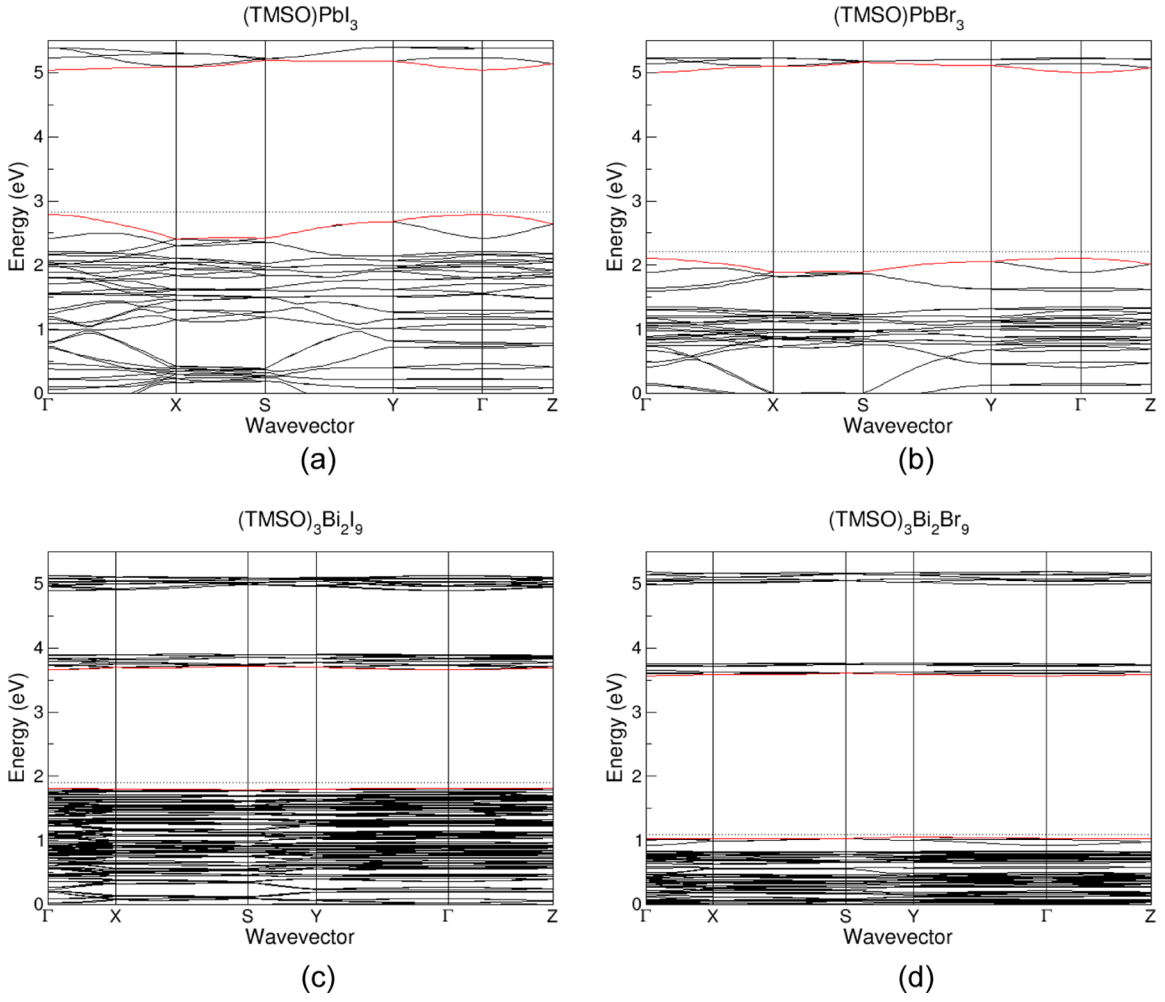

Figure 9. Band Structure of (a) $(TMSO)PbI_3$, (b) $(TMSO)PbBr_3$, (c) $(TMSO)_3Bi_2I_9$, and (d) $(TMSO)_3Bi_2Br_9$. Dotted lines represent the Fermi level of each compound.

Table 6. Band Gap Values (E_g) from Optical Reflectance Measurements (Exp) and from DFT Calculations[a]

	E_g (eV)		
samples	exp	SOC	no SOC
$(TMSO)PbI_3$	2.74	2.2	2.6
$(TMSO)_3Bi_2I_9$	2.11	1.8	2.8
$(TMSO)PbBr_3$	3.32	2.9	
$(TMSO)_3Bi_2Br_9$	2.80	2.5	

[a]Calculated values are reported with (SOC) or without (no SOC) spin−orbit coupling.

experimental values, the band gap decrease when substituting Pb with Bi is not correctly reproduced without SOC. The SOC is known to decrease the calculated band gap in this kind of structure,[74,75] and this trend is also verified for these systems. The inclusion of the SOC, therefore, allows reaching an entirely satisfactory qualitative and quantitative agreement. An accurate description of the relative difference is also obtained for the $(TMSO)PbBr_3$ and $(TMSO)_3Bi_2Br_9$ structures with the SOC calculations.

To investigate the influence of Pb/Bi and I/Br substitution on the electronic structure, the projected densities of states are compared across the four end members $(TMSO)PbX_3$ and $(TMSO)_3Bi_2X_9$ (Figure 10). The top of the valence band is

https://doi.org/10.1021/acs.jpcc.1c02571
J. Phys. Chem. C 2021, 125, 11728−11742

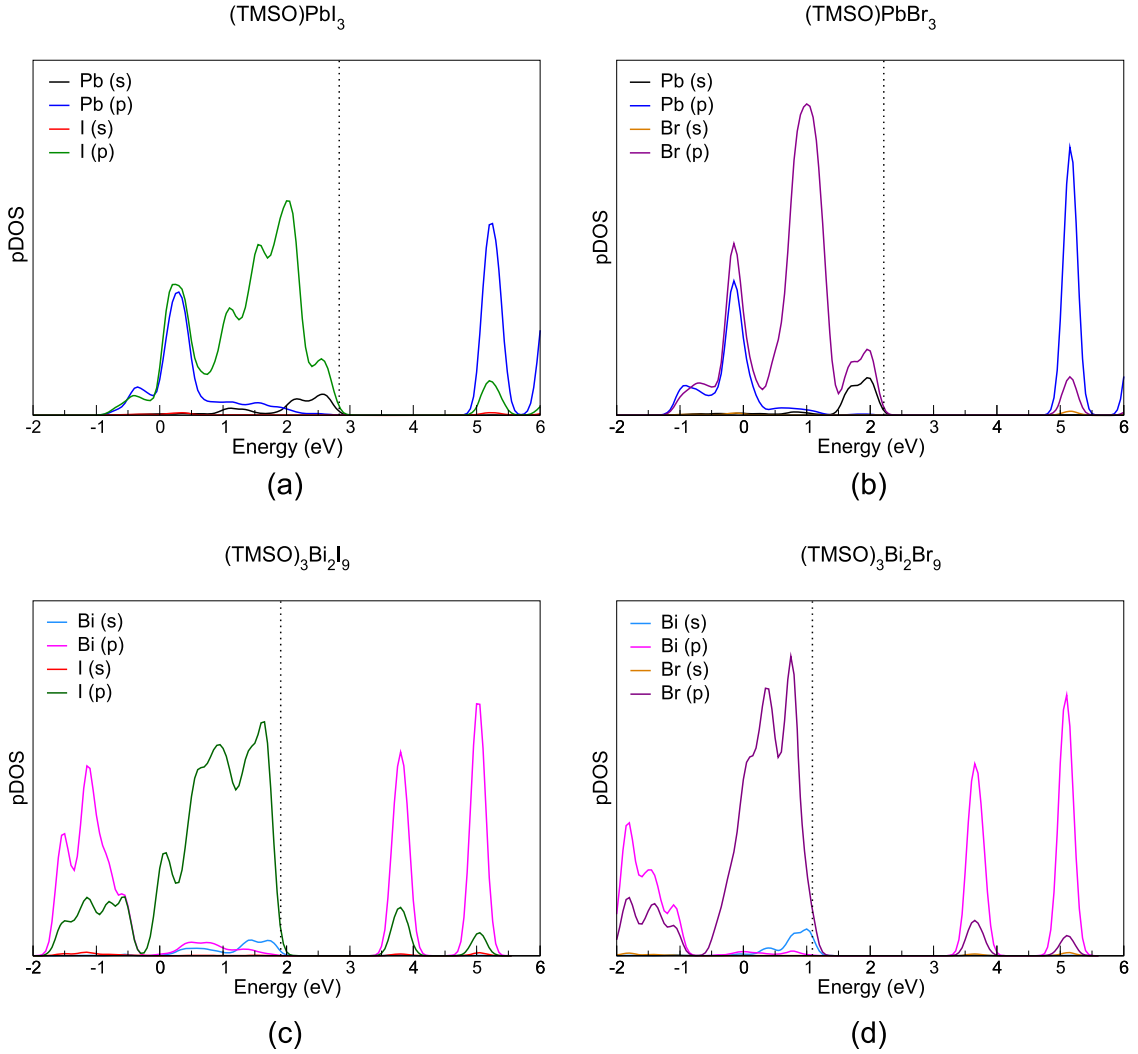

Figure 10. Projected density of states of (a) $(TMSO)PbI_3$, (b) $(TMSO)PbI_3$, (c) $(TMSO)_3Bi_2I_9$, and (d) $(TMSO)_3Bi_2Br_9$. Dotted lines represent the Fermi level of each compound.

mostly due to halide 4p/5p orbitals, with a minor contribution from 6s orbitals of Pb/Bi, while the bottom of the conduction band is mainly composed of the empty 6p orbitals of Pb/Bi. The substitution of Pb with Bi in the B site causes the lowering of the valence band of around 1 eV in both iodide and bromide compositions. In the conduction band, the p orbitals of the B-site cation lie at a lower energy in the bismuth-based samples. The combination of these two effects leads to a smaller band gap for the bismuth-containing end members. The halogen substitution from iodide to bromide lowers the energy of the valence band of about 0.6 eV (compared to the corresponding band gap increase of 0.7 eV). In contrast, the conduction band does not undergo any changes.

CONCLUSIONS

In the present work, the substitution of Pb^{2+} with Bi^{3+} in 1D hybrid pseudo-perovskites containing iodide and bromide anions has been deeply investigated, as what concerns the structure and optical absorption properties (both experimentally and through DFT simulations). Lead and bismuth ions share similar stereochemical preferences and similar crystal radii but, due to their different charges, neutrality is achieved through the insertion of vacant sites, obtained by elimination of Pb^{2+} sites. The extremely unusual peak shapes and widths of the X-ray diffraction peaks of mixed-metal phases—even trapezoidal in some cases—provided information about correlated and nonrandom distribution of the sequence of metal cations and vacancies, supported by a thermodynamic analysis of the mixing entropy and enthalpy contributions. For mixed-metal phases, a plateau in the enthalpy of mixing is able to explain well the evidence from diffraction measurements.

A complete structural, analytical, microscopic, and spectroscopic analysis of this new series of $(TMSO)_3Pb_{3x}Bi_{2(1-x)}X_9$ materials confirms that Bi^{3+} can easily substitute Pb^{2+}, forming solid solutions throughout the entire phase diagram, with either iodide and bromide compositions. The Bi^{3+} insertion, even at very low levels, is found to significantly lower the direct optical band gap, while bromide-containing samples display consistently higher band gap values. These observations are supported by periodic DFT simulations of the band structure.

ASSOCIATED CONTENT

Supporting Information

The Supporting Information is available free of charge at https://pubs.acs.org/doi/10.1021/acs.jpcc.1c02571.

https://doi.org/10.1021/acs.jpcc.1c02571
J. Phys. Chem. C 2021, 125, 11728−11742

Experimental details; elemental quantification using different methods; crystal data; predicted lattice parameters determined using different functionals; Rietveld refinements of doped samples; electron micrographs; thermal analysis; Tauc plots; and defect mixing thermodynamics of doped samples (PDF)

AUTHOR INFORMATION

Corresponding Authors

Francesco Giannici − *Dipartimento di Fisica e Chimica "Emilio Segrè", Università di Palermo, 90128 Palermo, Italy;* orcid.org/0000-0003-3086-956X; Email: francesco.giannici@unipa.it

Norberto Masciocchi − *Dipartimento di Scienza e Alta Tecnologia & To.Sca.Lab., Università dell'Insubria, 22100 Como, Italy;* orcid.org/0000-0001-9921-2350; Email: norberto.masciocchi@uninsubria.it

Authors

Candida Pipitone − *Dipartimento di Fisica e Chimica "Emilio Segrè", Università di Palermo, 90128 Palermo, Italy*

Antonino Martorana − *Dipartimento di Fisica e Chimica "Emilio Segrè", Università di Palermo, 90128 Palermo, Italy;* orcid.org/0000-0003-1911-1627

Gonzalo García-Espejo − *Dipartimento di Scienza e Alta Tecnologia & To.Sca.Lab., Università dell'Insubria, 22100 Como, Italy;* orcid.org/0000-0002-2545-1954

Silvia Carlotto − *Dipartimento di Scienze Chimiche, Università di Padova and Institute of Condensed Matter Chemistry and Technologies for Energy (ICMATE), National Research Council (CNR), 35131 Padova, Italy;* orcid.org/0000-0003-0043-3538

Maurizio Casarin − *Dipartimento di Scienze Chimiche, Università di Padova and Institute of Condensed Matter Chemistry and Technologies for Energy (ICMATE), National Research Council (CNR), 35131 Padova, Italy;* orcid.org/0000-0002-3347-8751

Antonietta Guagliardi − *Istituto di Cristallografia & To.Sca.Lab., Consiglio Nazionale delle Ricerche, 22100 Como, Italy;* orcid.org/0000-0001-6390-2114

Complete contact information is available at: https://pubs.acs.org/10.1021/acs.jpcc.1c02571

Notes

The authors declare no competing financial interest.

ACKNOWLEDGMENTS

This project was partially supported by MIUR (PRIN-2017L8WW48, Project HY-TEC) and by the University of Padova (grant: P-DISC #CARL-SID17 BIRD2017-UNIPD, project CHIRoN). We thank the following from Università di Palermo: S. Cataldo, R. Lo Brutto, and A. Pettignano for the ICP-OES measurements, and G. Lazzara for useful discussions. We acknowledge the CINECA award under the ISCRA initiative, for the availability of high-performance computing resources and support (project IsC83_1HyPe). The Computational Chemistry Community (C_3P) of the University of Padova is kindly acknowledged. We thank one anonymous reviewer for providing interesting cues for discussion.

REFERENCES

(1) Green, M. A.; Ho-Baillie, A. Perovskite Solar Cells: The Birth of a New Era in Photovoltaics. *ACS Energy Lett.* **2017**, *2*, 822−830.

(2) Zhang, J.; Zhang, W.; Cheng, H.-M.; Silva, S. R. P. Critical Review of Recent Progress of Flexible Perovskite Solar Cells. *Mater. Today* **2020**, 68−88.

(3) Ansari, M. I. H.; Qurashi, A.; Nazeeruddin, M. K. Frontiers, Opportunities, and Challenges in Perovskite Solar Cells: A Critical Review. *J. Photochem. Photobiol., C* **2018**, *35*, 1−24.

(4) Haque, M. A.; Kee, S.; Villalva, D. R.; Ong, W.; Baran, D. Halide Perovskites: Thermal Transport and Prospects for Thermoelectricity. *Adv. Sci.* **2020**, *7*, 1903389−1903410.

(5) Liu, X.-K.; Xu, W.; Bai, S.; Jin, Y.; Wang, J.; Friend, R. H.; Gao, F. Metal Halide Perovskites for Light-Emitting Diodes. *Nat. Mater.* **2021**, *20*, 10−21.

(6) Wu, T.; Pisula, W.; Rashid, M. Y. A.; Gao, P. Application of Perovskite-Structured Materials in Field-Effect Transistors. *Adv. Electron. Mater.* **2019**, *5*, 1900444−1900467.

(7) Das, S.; Gholipour, S.; Saliba, M. Perovskites for Laser and Detector Applications. *Energy Environ. Mater.* **2019**, *2*, 146−153.

(8) Zhou, F.; Li, Z.; Lan, W.; Wang, Q.; Ding, L.; Jin, Z. Halide Perovskite, a Potential Scintillator for X-Ray Detection. *Small Methods* **2020**, *10*, No. 2000506.

(9) Hu, Z.; Lin, Z.; Su, J.; Zhang, J.; Chang, J.; Hao, Y. A Review on Energy Band-Gap Engineering for Perovskite Photovoltaics. *Sol. RRL* **2019**, *3*, 1900304−1900313.

(10) Yang, Z.; Rajagopal, A.; Jen, A. K.-Y. Ideal Bandgap Organic-Inorganic Hybrid Perovskite Solar Cells. *Adv. Mater.* **2017**, *29*, 1704418.

(11) He, S.; Qiu, L.; Ono, L. K.; Qi, Y. How Far Are We from Attaining 10-Year Lifetime for Metal Halide Perovskite Solar Cells? *Mater. Sci. Eng., R* **2020**, *140*, 100545−100580.

(12) Bryant, D.; Aristidou, N.; Pont, S.; Sanchez-Molina, I.; Chotchunangatchaval, T.; Wheeler, S.; Durrant, J. R.; Haque, S. A. Light and Oxygen Induced Degradation Limits the Operational Stability of Methylammonium Lead Triiodide Perovskite Solar Cells. *Energy Environ. Sci.* **2016**, *9*, 1655−1660.

(13) Li, W.-G.; Rao, H.-S.; Chen, B.-X.; Wang, X.-D.; Kuang, D.-B. Formamidinium-Methylammonium Lead Iodide Perovskite Single Crystal Exhibits Exceptional Optoelectronic Properties and Longterm Stability. *J. Mater. Chem. A* **2017**, *5*, 19431−19438.

(14) Noh, J. H.; Im, S. H.; Heo, J. H.; Mandal, T. N.; Seok, S. I. Chemical Management for Colorful, Efficient, and Stable Inorganic−Organic Hybrid Nanostructured Solar Cells. *Nano Lett.* **2013**, *13*, 1764−1769.

(15) Zhou, Y.; Chen, J.; Bakr, O. M.; Sun, H.-T. Metal-Doped Lead Halide Perovskites: Synthesis, Properties, and Optoelectronic Applications. *Chem. Mater.* **2018**, *30*, 6589−6613.

(16) Tang, W.; Zhang, J.; Ratnasingham, S.; Liscio, F.; Chen, K.; Liu, T.; Wan, K.; Galindez, E. S.; Bilotti, E.; Reece, M.; et al. Substitutional Doping of Hybrid Organic−Inorganic Perovskite Crystals for Thermoelectrics. *J. Mater. Chem. A* **2020**, *8*, 13594−13599.

(17) Zhou, Y.; Yong, Z.-J.; Zhang, K.-C.; Liu, B.-M.; Wang, Z.-W.; Hou, J.-S.; Fang, Y.-Z.; Zhou, Y.; Sun, H.-T.; Song, B. Ultrabroad Photoluminescence and Electroluminescence at New Wavelengths from Doped Organometal Halide Perovskites. *J. Phys. Chem. Lett.* **2016**, *7*, 2735−2741.

(18) Mir, W. J.; Jagadeeswararao, M.; Das, S.; Nag, A. Colloidal Mn-Doped Cesium Lead Halide Perovskite Nanoplatelets. *ACS Energy Lett.* **2017**, *2*, 537−543.

(19) Zhou, C.; et al. Low Dimensional Metal Halide Perovskites and Hybrids. *Mater. Sci. Eng., R* **2019**, *137*, 38−65.

(20) Elsenety, M. M.; Antoniadou, M.; Balis, N.; Kaltzoglou, A.; Sygellou, L.; Stergiou, A.; Tagmatarchis, N.; Falaras, P. Stability Improvement and Performance Reproducibility Enhancement of Perovskite Solar Cells Following $(FA/MA/Cs)PbI_{3-x}Br_x/(CH_3)_3SPbI_3$ Dimensionality Engineering. *ACS Appl. Energy Mater.* **2020**, *3*, 2465−2477.

(21) Yao, Q.; Xue, Q.; Li, Z.; Zhang, K.; Zhang, T.; Li, N.; Yang, S.; Brabec, C. J.; Yip, H.; Cao, Y. Graded 2D/3D Perovskite Heterostructure for Efficient and Operationally Stable MA-Free Perovskite Solar Cells. *Adv. Mater.* **2020**, *32*, 2000571−2000581.
(22) Zhu, P.; Zhu, J. Low-dimensional Metal Halide Perovskites and Related Optoelectronic Applications. *InfoMat* **2020**, *2*, 341−378.
(23) Jin, X.; Lv, C.; Zhou, X.; Ye, L.; Xie, H.; Liu, Y.; Su, H.; Zhang, B.; Chen, G. Oxygen Vacancy Engineering of $Bi_{24}O_{31}Cl_{10}$ for Boosted Photocatalytic CO_2 Conversion. *ChemSusChem* **2019**, *12*, 2740−2747.
(24) Zhou, C.; Tian, Y.; Khabou, O.; Worku, M.; Zhou, Y.; Hurley, J.; Lin, H.; Ma, B. Manganese-Doped One-Dimensional Organic Lead Bromide Perovskites with Bright White Emissions. *ACS Appl. Mater. Interfaces* **2017**, *9*, 40446−40451.
(25) Liu, X.; Xu, X.; Li, B.; Liang, Y.; Li, Q.; Jiang, H.; Xu, D. Antimony-Doping Induced Highly Efficient Warm-White Emission in Indium-Based Zero-Dimensional Perovskites. *CCS Chem.* **2020**, *2*, 216−224.
(26) Cortecchia, D.; Mróz, W.; Neutzner, S.; Borzda, T.; Folpini, G.; Brescia, R.; Petrozza, A. Defect Engineering in 2D Perovskite by Mn(II) Doping for Light-Emitting Applications. *Chem* **2019**, *5*, 2146−2158.
(27) Dutta, S. K.; Dutta, A.; Das Adhikari, S.; Pradhan, N. Doping Mn^{2+} in Single-Crystalline Layered Perovskite Microcrystals. *ACS Energy Lett.* **2019**, *4*, 343−351.
(28) Li, H.; Wang, X.; Zhang, T.; Gong, X.; Sun, Q.; Pan, H.; Shen, Y.; Ahmad, S.; Wang, M. Layered Ruddlesden−Popper Efficient Perovskite Solar Cells with Controlled Quantum and Dielectric Confinement Introduced via Doping. *Adv. Funct. Mater.* **2019**, *29*, 1903292−1903293.
(29) Bakthavatsalam, R.; Biswas, A.; Chakali, M.; Bangal, P. R.; Kore, B. P.; Kundu, J. Temperature-Dependent Photoluminescence and Energy-Transfer Dynamics in Mn^2-Doped $(C_4H_9NH_3)_2PbBr_4$ Two-Dimensional (2D) Layered Perovskite. *J. Phys. Chem. C* **2019**, *123*, 4739−4748.
(30) David, W. I. F.; Shankland, K.; McCusker, L. B.; Baerlocher, C. International Union of Crystallography Monographs on Crystallography. In *Structure Determination from Powder Diffraction Data*; Oxford University Press, 2006.
(31) David, B. *Structure Determination from Powder Diffraction Data*, CPD Newsletters #25; International Union of Crystallography, 2001; pp 1−36.
(32) Masciocchi, N. *Powder Diffraction of Molecular Functional Materials*, CPD Newsletters #31; International Union of Crystallography, 2004; pp 1−77.
(33) Coelho, A. A. Indexing of Powder Diffraction Patterns by Iterative Use of Singular Value Decomposition. *J. Appl. Crystallogr.* **2003**, *36*, 86−95.
(34) *TOPAS_R*, v.3.0; Bruker AXS: Karlsruhe, Germany, 2005.
(35) Cheary, R. W.; Coelho, A. A Fundamental Parameters Approach to X-Ray Line-Profile Fitting. *J. Appl. Crystallogr.* **1992**, *25*, 109−121.
(36) Dollase, W. A. Correction of Intensities for Preferred Orientation in Powder Diffractometry: Application of the March Model. *J. Appl. Crystallogr.* **1986**, *19*, 267−272.
(37) Giannozzi, P.; Baseggio, O.; Bonfà, P.; Brunato, D.; Car, R.; Cavazzoni, C.; de Gironcoli, S.; Delugas, P.; Ruffino, F. F.; Ferretti, A.; et al. Quantum ESPRESSO toward the Exascale. *J. Chem. Phys.* **2020**, *152*, 154105−154116.
(38) Giannozzi, P.; Baroni, S.; Bonini, N.; Calandra, M.; Car, R.; Cavazzoni, C.; Ceresoli, D.; Chiarotti, G. L.; Cococcioni, M.; Dabo, I.; et al. QUANTUM ESPRESSO: A Modular and Open-Source Software Project for Quantum Simulations of Materials. *J. Phys.: Condens. Matter* **2009**, *21*, 395502−395521.
(39) Giannozzi, P.; Andreussi, O.; Brumme, T.; Bunau, O.; Buongiorno, M.; Calandra, M.; Car, R.; Cavazzoni, C.; Ceresoli, D.; Cococcioni, M.; et al. Advanced Capabilities for Materials Modelling with Quantum ESPRESSO. *J. Phys.: Condens. Matter* **2017**, *29*, 465901−465931.
(40) Anisimov, V. I.; Zaanen, J.; Andersen, O. K. Band Theory and Mott Insulators: Hubbard *U* Instead of Stoner *I*. *Phys. Rev. B* **1991**, *44*, 943−954.
(41) Perdew, J. P.; Burke, K.; Ernzerhof, M. Generalized Gradient Approximation Made Simple. *Phys. Rev. Lett.* **1996**, *77*, 3865−3868.
(42) Blöchl, P. E. Projector Augmented-Wave Method. *Phys. Rev. B* **1994**, *50*, 17953−17979.
(43) Jiang, J.; et al. Carrier Lifetime Enhancement in Halide Perovskite via Remote Epitaxy. *Nat. Commun.* **2019**, *10*, No. 4145.
(44) Bertolotti, F.; Protesescu, L.; Kovalenko, M. V.; Yakunin, S.; Cervellino, A.; Billinge, S. J. L.; Terban, M. W.; Pedersen, J. S.; Masciocchi, N.; Guagliardi, A. Coherent Nanotwins and Dynamic Disorder in Cesium Lead Halide Perovskite Nanocrystals. *ACS Nano* **2017**, *11*, 3819−3831.
(45) Li, C.; Guerrero, A.; Huettner, S.; Bisquert, J. Unravelling the Role of Vacancies in Lead Halide Perovskite through Electrical Switching of Photoluminescence. *Nat. Commun.* **2018**, *9*, No. 5113.
(46) Kim, J.; Lee, S.-H.; Lee, J. H.; Hong, K.-H. The Role of Intrinsic Defects in Methylammonium Lead Iodide Perovskite. *J. Phys. Chem. Lett.* **2014**, *5*, 1312−1317.
(47) Walsh, A.; Scanlon, D. O.; Chen, S.; Gong, X. G.; Wei, S.-H. Self-Regulation Mechanism for Charged Point Defects in Hybrid Halide Perovskites. *Angew. Chem., Int. Ed.* **2015**, *54*, 1791−1794.
(48) Hofmann, D. W. M. Fast Estimation of Crystal Densities. *Acta Crystallogr., Sect. B: Struct. Sci.* **2002**, *B57*, 489−493.
(49) Wang, K.; Jin, Z.; Liang, L.; Bian, H.; Bai, D.; Wang, H.; Zhang, J.; Wang, Q.; Liu, S. All-Inorganic Cesium Lead Iodide Perovskite Solar Cells with Stabilized Efficiency beyond 15%. *Nat. Commun.* **2018**, *9*, No. 4544.
(50) Aebli, M.; Benin, B.; McCall, K. M.; Viktoriia, M.; Thöny, D.; Grützmacher, H.; Kovalenko, M. V. White $CsPbBr_3$: Characterizing the One-Dimensional Cesium Lead Bromide Polymorph. *Helv. Chim. Acta* **2020**, *103*, No. e20000080.
(51) Kaltzoglou, A.; Stoumpos, C. C.; Kontos, A. G.; Manolis, G. K.; Papadopoulos, K.; Papadokostaki, K. G.; Psycharis, V.; Tang, C. C.; Jung, Y.-K.; Walsh, A.; et al. Trimethylsulfonium Lead Triiodide: An Air-Stable Hybrid Halide Perovskite. *Inorg. Chem.* **2017**, *56*, 6302−6309.
(52) Jin, Z.; Zhang, Z.; Xiu, J.; Wen, Z.; Song, H.; Gatti, T.; He, Z. A Critical Review on Bismuth and Antimony Halides Based Perovskites and Derivatives for Photovoltaic Applications: Recent Advances and Challenges. *J. Mater. Chem. A* **2020**, *8*, 16166−16188.
(53) Shannon, R. D. Revised Effective Ionic Radii and Systematic Studies of Interatomic Distances in Halides and Chalcogenides. *Acta Crystallogr., Sect. A: Found. Adv.* **1976**, *A32*, 751−768.
(54) Pipitone, C.; Giannici, F.; Martorana, A.; Bertolotti, F.; Calabrese, G.; Milita, S.; Guagliardi, A.; Masciocchi, N. Proton Sponge Lead Halides Containing 1D Polyoctahedral Chains. *CrystEngComm* **2021**, *23*, 1126−1139.
(55) Willey, R.; Ravindran, M.; Drew, M. G. Reactions of Trimethylamine with Mn(I1) and Cd(I1) Chlorides: Crystal and Molecular Structure of $[Me_3NH][MnCl_3]$. *Inorg. Chim. Acta* **1990**, *175*, 99−103.
(56) Chapuis, G.; Zuniga, F. J. Solid-Solid Phase Transitions in $[NH(CH_3)_3]CdCl_3$. *Acta Crystallogr., Sect. B: Struct. Crystallogr. Cryst. Chem.* **1980**, *B36*, 807−812.
(57) Puget, R.; Jannin, M.; de Brauer, C.; Perret, R. Structures of Trimethyloxosulfonium Salts. V. The Catena-Tri-μ-Chloro-Cadmate and the Catena-Tri-μ-Bromo-Cadmate. *Acta Crystallogr., Sect. C: Cryst. Struct. Commun.* **1991**, *47*, 1803−1805.
(58) De Brauer, C.; Kolinsky, C.; Jannin, M.; Puget, R. Trimethyloxosulfonium Salts. IX. Study of Some Mixed Compounds, $(CH3)_3SOCdCl_{3-x}Br_x$. *Acta Crystallogr., Sect. C: Cryst. Struct. Commun.* **1996**, *52*, 812−817.
(59) Nakashima, K.; Kawaguchi, Y. A New Method for Analysing Peak Broadening Caused by Compositional Fluctuation in X-Ray Diffraction Measurements. *J. Appl. Crystallogr.* **2001**, *34*, 681−690.
(60) Alexandridis, P.; Hatton, T. A. Poly(Ethylene Oxide)-Poly-(Propylene Oxide)-Poly (Ethylene Oxide) Block Copolymer Surfactants in Aqueous Solutions and at Interfaces: Thermodynamics, Structure, Dynamics, and Modeling. *Colloids Surf., A* **1995**, *96*, 1−46.

https://doi.org/10.1021/acs.jpcc.1c02571
J. Phys. Chem. C 2021, 125, 11728−11742

(61) Longo, A.; Sciortino, L.; Giannici, F.; Martorana, A. Crossing the Boundary between Face-Centred Cubic and Hexagonal Close Packed: The Structure of Nanosized Cobalt Is Unraveled by a Model Accounting for Shape, Size Distribution and Stacking Faults, Allowing Simulation of XRD, XANES and EXAFS. *J. Appl. Crystallogr.* **2014**, *47*, 1562−1568.
(62) Konings, R. J. M.; Kok-Scheele, A.; Cordfunke, E. H. P. On the Phase Diagrams of the Systems Pb-PbI_2, PbI_2-NaI and PbI_2-ZnI_2. *Thermochim. Acta* **1995**, *261*, 221−225.
(63) Konings, R. J. M.; Cordfunke, E. H. P.; van der Laan, R. R. Enthalpy Increment Measurements of PbI_2: Evidence for a Reversible Polytypic Transition. *J. Alloys Compd.* **1995**, *230*, 85−88.
(64) Minagawa, T. Common Polytypes of PbI_2 at Low and High Temperatures and the 2*H*−12*R*. *Acta Crystallogr., Sect. A: Found. Adv.* **1975**, *A31*, 823−824.
(65) Dmitriev, Y. N.; Bennett, P. R.; Cirignano, L. J.; Gupta, T. K.; Klugerman, M.; Shah, K. S. Solid Solutions $(PbI_2)_x$−$(BiI_3)_{1-x}$. *MRS Proc.* **1999**, *580*, 99−104.
(66) Vertegel, I. G.; Chesnokov, E. D.; Ovcharenko, O. I.; Ivanova, L. S.; Gnatenko, YuP.; Vertegel, I. I. I^{127} NQR Spectra of $Pb_{1-x}Cd_xI_2$ and $(BiI_3)_{(1-x)}(PbI_2)_x$ of Mixed Layered Semiconductors. *Semicond. Phys., Quantum Electron. Optoelectron.* **2017**, *20*, 340−343.
(67) Barabash, O. I.; Vertegel, I. G.; Chesnokov, E. D.; Ovcharenko, O. I.; Ivanova, L. S. Symmetry Peculiarities of the Intracrystalline Fields Layered Semiconductor Crystals $(PbI_2)_{(1-x)}(BiI_3)_x$. *Funct. Mater.* **2012**, *19*, 330−333.
(68) Nitsch, K.; Rodová, M. Differential Thermal Analysis Study of Lead Bromide. *J. Cryst. Growth* **1993**, *134*, 386−387.
(69) Gerisch, A.; Ruck, M. $(Bi_9)_4[Bi_3Pb_9Br_{47}]$: Probing the Limits of the Concept "Crystal". *Z. Kristallogr.* **2011**, *226*, 613−618.
(70) Miao, X.; Qiu, T.; Zhang, S.; Ma, H.; Hu, Y.; Bai, F.; Wu, Z. Air-Stable $CsPb_{1-x}Bi_xBr_3$ ($0 \le x \ll 1$) Perovskite Crystals: Optoelectronic and Photostriction Properties. *J. Mater. Chem. C* **2017**, *5*, 4931−4939.
(71) Hu, Y.; Bai, F.; Liu, X.; Ji, Q.; Miao, X.; Qiu, T.; Zhang, S. Bismuth Incorporation Stabilized α-$CsPbI_3$ for Fully Inorganic Perovskite Solar Cells. *ACS Energy Lett.* **2017**, *2*, 2219−2227.
(72) Abdelhady, A. L.; Saidaminov, M. I.; Murali, B.; Adinol, V.; Voznyy, O.; Katsiev, K.; Alarousu, E.; Comin, R.; Dursun, I.; Sinatra, L.; Sargent, E. H.; Mohammed, O. F.; Bakr, O. M. Heterovalent Dopant Incorporation for Bandgap and Type Engineering of Perovskite Crystals. *J. Phys. Chem. Lett.* **2016**, *7*, 295−301.
(73) Soykan, C.; Gocmez, H. The Physical Properties of Bismuth Replacement in Lead Halogen Perovskite Solar Cells: $CH_3NH_3Pb_{1-x}Bi_xI_3$ Compounds by Ab-Initio Calculations. *Results Phys.* **2019**, *13*, 102278−102288.
(74) Pazoki, M.; Johansson, M. B.; Zhu, H.; Broqvist, P.; Edvinsson, T.; Boschloo, G.; Johansson, E. M. J. Bismuth Iodide Perovskite Materials for Solar Cell Applications: Electronic Structure, Optical Transitions, and Directional Charge Transport. *J. Phys. Chem. C* **2016**, *120*, 29039−29046.
(75) Even, J.; Pedesseau, L.; Jancu, J.-M.; Katan, C. Importance of Spin−Orbit Coupling in Hybrid Organic/Inorganic Perovskites for Photovoltaic Applications. *J. Phys. Chem. Lett.* **2013**, *4*, 2999−3005.

https://doi.org/10.1021/acs.jpcc.1c02571
J. Phys. Chem. C 2021, 125, 11728−11742